Journal of Materials Chemistry A

ROYAL SOCIETY OF CHEMISTRY

PAPER

View Article Online
View Journal | View Issue



Cite this: J. Mater. Chem. A, 2023, 11, 12223

# Self-powered $NH_3$ synthesis by trifunctional $Co_2B$-based high power density Zn–air batteries†

Divyani Gupta, [a] Alankar Kafle,[a] Prajna Parimita Mohanty,[bc] Tisita Das, [c] Sudip Chakraborty, [c] Rajeev Ahuja [bd] and Tharamani C. Nagaiah [*a]

Received 11th April 2023
Accepted 17th May 2023

DOI: 10.1039/d3ta02178e

rsc.li/materials-a



The electrochemical production of $NH_3$ by Zn–air batteries is a viable and economical approach to realize sustainable and competent energy conversion. We report the environment friendly, cost-effective, and energy efficient sonochemical synthesis of amorphous $Co_2B$ nanosheets for trifunctional electrocatalysis. The catalyst exhibits a high $NH_3$ yield rate (2.98 mg $h^{-1}$ $mg_{cat.}^{-1}$), F.E (20.45%), and TOF of 0.74 $h^{-1}$ at −0.3 V *vs.* RHE, thereby unveiling an outstanding performance for the artificial ammonia synthesis. The reliable and true $NH_3$ production is premediated by following rigorous protocol that involves the purification of gas supplies, elimination of N-contaminants, and quantification of $NH_3$ by different methods, UV-Vis spectroscopy and $^{15}N_2$ isotope labelling experiments. More interestingly, DFT calculations on the $Co_2B$ catalyst surface shed light on the efficient NRR owing to the presence of Co active sites and possible HER suppression. The optimized $Co_2B$ catalyst shows outstanding oxygen bifunctional activity. When employed as an air-cathode for Zn–air batteries, it exhibited remarkable electrocatalytic activity delivering an open circuit potential of 1.45 V with a high power density of 500 mW $cm^{-2}$ and an energy density of 1078 W h $kg^{-1}$, which can perform $NH_3$ generation with an overall $NH_3$ production yield rate of 1.048 mg $h^{-1}$ $mg_{cat.}^{-1}$.

## Introduction

There are exigent demands to develop efficient and robust electrochemical energy conversion and storage devices to muddle through future energy crises and environmental pollution.[1] The $N_2$ cycle ($N_2$/$NH_3$, *i.e.* $N_2$ fixation) is a crucial process for humans to lead a sustainable life on earth because the produced ammonia provides food to a huge percentage of the world's population, can store hydrogen indirectly, and act as a carbon free energy carrier.[2] Amid different technologies for artificial $N_2$ fixation, a century-old Haber–Bosch process[3] is applied for the large scale production of ammonia, which is highly energy intensive (about 1–3% world's energy consumption), operates at high temperatures (400–500 °C) and pressure (100–200 atm), and consumes excessive natural gas (*e.g.*, $CH_4$ for $H_2$ production; 3–5% world's natural gas production).[4] Above all, it is accompanied by immense carbon emissions responsible for around 1.5% of greenhouse gas production averaging about 2.9 tons $CO_2$ per ton of $NH_3$ globally.[5,6] Consequently, it is critical to deal with severe energy and environmental concerns raised due to the traditional Haber–Bosch process.[7] The development of cost-effective and energy efficient alternative technologies with renewable energy sources is of great interest.[8,9] In recent years, the conversion of abundant $N_2$ to $NH_3$ *via* an electrochemical pathway has gained significant attention owing to the ease of operation under ambient conditions using water as a source of $H_2$ and renewable energy source derived electric power supply subsequently without $CO_2$ emissions.[5,10,11]

In addition, the utilization of high-power density rechargeable metal–air batteries *viz.* Zn (ZAB) for electrochemical ammonia synthesis[12] is a game-changing strategy because of the earth's abundant, economical and environment friendly metal anode and its high theoretical energy density that is three times higher than that of Li-ion batteries (1216 W h $kg^{-1}$).[13] More importantly, integrating ZAB in electrochemical $NH_3$ production provides cumulative efficiency compared to its device.[14,15] To accomplish these necessities, the principal task is to develop highly efficient and robust catalysts active towards nitrogen reduction reaction and oxygen bifunctional catalyst *viz.* oxygen reduction reaction (ORR) and oxygen evolution reaction (OER) for ZAB.[16] For Zn–air batteries, the degradation of air cathodes during consecutive cycling due to the sluggish multielectron

[a]Department of Chemistry, Indian Institute of Technology Ropar, Rupnagar, Punjab 140001, India. E-mail: tharamani@iitrpr.ac.in

[b]Department of Physics, Indian Institute of Technology Ropar, Rupnagar, Punjab 140001, India

[c]Materials Theory for Energy Scavenging (MATES) Lab, Harish-Chandra Research Institute (HRI) Allahabad, HBNI, Chhatnag Road, Jhunsi, Prayagraj, Allahabad 211019, India

[d]Condensed Matter Theory Group, Department of Physics and Astronomy, Uppsala University, Uppsala, SE-75120, Sweden

† Electronic supplementary information (ESI) available. See DOI: https://doi.org/10.1039/d3ta02178e

process of OER and ORR remains the major disadvantage.[17] Similarly, the adsorption and activation of strong N≡N triple bond with high dissociation binding energy of 940.95 kJ $mol^{-1}$, negative $e^-$ affinity of −1.8 eV, high ionization potential of 15.8 eV, high HOMO–LUMO gap of 10.82 eV and the permanent dipole is a prerequisite for the efficacious synthesis of $NH_3$.[18] To date, precious Pt/C is the state-of-art ORR catalysts but are not efficient towards OER/NRR. However, $IrO_2/RuO_2$ is the benchmark OER catalyst but is not efficient for ORR/NRR.[19–21]

Henceforth, the primary challenge for sustainable and renewable energy is the discovery and design of efficient electrocatalysts exhibiting superior trifunctional activity for NRR and rechargeable ZABs with improved stability during their operation.[22] More specifically, the expensive, scarce nature of noble metal-based state-of-art catalysts along with their sluggish kinetics impede their real-time application. This limitation demands the development of a cost-effective non-noble metal-based catalyst for OER, ORR and NRR, which holds the potential to compete with or even surpass the activity of precious benchmark catalysts.[23,24] Moreover, the designing of such a catalyst, which possesses an ample number of active sites and robustness towards three reactions with completely different fundamental mechanisms, is yet complicated but the need of the hour.[25–28] However, so far, only three reports are available wherein ZABs have been used to power electrochemical $NH_3$ synthesis.[12,29,30] Several classes of catalysts, including noble-metal-based,[31–33] non-noble metal-based[34,35] and metal free-based catalysts,[36–38] have been explored towards NRR in aqueous media, but the faradaic efficiency (F.E.) and $NH_3$ production yield rate obstruct their attempt to be put into practice.[39–41] Therefore, the development of suitable, cost-effective and active catalysts is vital to achieving good bifunctional activity.[24] In the past decade, extensive efforts have been devoted to developing precious metal free oxygen bifunctional catalysts,[42–46] including transition-metal oxides/hydroxides, sulphides, carbides, carbonaceous materials, molecular catalysts, nitrides, and phosphides.[47–50] Transition metal borides (TMBs) have begun to appear as an important inorganic class of materials with wide-spread applications in various fields, such as energy storage,[51,52] energy conversion,[53] superconductivity, and thermoelectricity.[54] TMBs, including cobalt and nickel, have been generally used in electrocatalysis because of their enhanced electrical conductivity, stability and hardness.[55,56] TMBs exhibit superior oxygen evolution reaction (OER) performance in alkaline media compared with noble metal catalysts, metal oxides, and metal alloy counterparts.[57] Very recently, $Co_2B$ was explored in a report by Jose *et al.*[58] for the ORR in alkaline media to achieve higher activity than the benchmark catalyst. In addition, several theoretical studies have reported the potential of TMBs for the NRR.[59–63] For now, there are very limited reports on TMBs for oxygen bifunctional electrocatalysis[64–66] because of the complicated synthesis of TMBs relying on expensive methods such as physical/chemical vapor deposition, high-energy ball milling, and arc-plasma. These methods usually involve toxic gaseous precursors, and/or complex procedures as well as high-cost devices, incurring the problem of practical applicability.[54,67] Therefore, in this study, we exploit a cost-effective, energy efficient, less time consuming, and facile sonochemical approach for the synthesis of TMBs.[68,69] Moreover, this approach has the advantage of obstructing particle agglomeration under a chemical environment[70] owing to ultrasound waves generated during sonochemical synthesis.

Herein, we report the synthesis of amorphous cobalt boride with porous nanosheet morphology as a trifunctional catalyst for NRR, ORR, and OER under ambient conditions. The optimized cobalt boride was equipped in a Zn–air battery as an air cathode and successfully powered a self-driven $NH_3$ synthesis. To the best of our knowledge, this is the first report to explore metal borides as a trifunctional catalyst for battery-driven $NH_3$ synthesis under ambient conditions. The catalyst shows good activity towards electrochemical $NH_3$ synthesis with F.E. of 20.45% in alkaline media at −0.3 V *vs.* RHE. When employed as an air-cathode catalyst for Zn–air battery, $Co_2B$ exhibits remarkable electrocatalytic activity, delivering open circuit potential of 1.45 V with a high-power density of 500 mW $cm^{-2}$ and an energy density of 1078 W h $kg^{-1}$, which can carry out $NH_3$ generation with an overall $NH_3$ production yield rate of 1.048 mg $h^{-1}$ $mg_{cat.}{}^{-1}$.

## Results and discussion

The $Co_2B$ catalysts were prepared using a green and facile sonochemical approach with cobalt chloride and $NaBH_4$ (Scheme 1) under an inert atmosphere. Briefly, the dropwise addition of aq. $NaBH_4$ aqueous solution was carried out into aq. $CoCl_2$ solution under continuous bath sonication and probe sonication at regular intervals (details are in ESI†) with a probe frequency of 20 Hz. To understand the effect of boron on the morphology, microstructure thence trifunctional activity, three variants of cobalt boride were synthesized by varying the ratio of cobalt chloride to $NaBH_4$ designated as $Co_2B$ (1 : 4/1 : 8/1 : 12).

### Electrochemical dinitrogen reduction (NRR)

To understand the potential efficacy of the synthesized catalyst towards electrocatalytic NRR, linear sweep voltammograms (LSV) were recorded in Ar and $N_2$-saturated 0.1 M KOH electrolytes. Because of any impurities present in the Ar or $N_2$ gas feed streams, we purified the gas with $KMnO_4$ and $H_2SO_4$ trap prior to NRR measurements (Fig. S1, ESI†).[71] LSV for $Co_2B$ catalysts exhibit a distinct increase in cathodic current density under an $N_2$ atmosphere than in Ar-saturated electrolytes (Fig. 1a and S2, ESI†). $Co_2B$ (1 : 8) demonstrates a higher current density, which suggests pronounced activity of the same for NRR than other composites. Under the continuous $N_2$ gas flow in the cathode compartment of the H-cell, $N_2$ on the surface of $Co_2B$ catalysts react with $H^+$ ions to form $NH_3$ with potentiostatic reduction, wherein the chronoamperometry was performed for 2 h (Fig. S3, ESI†). The quantification of the $NH_3$ formed during the reaction was performed by applying the indophenol blue method (Fig. S4 and S5A, ESI†).[45] As shown in Fig. S4,† the highest faradaic efficiency (F.E.) of 20.45% and $NH_3$ yield of 2980.22 μg $h^{-1}$ $mg_{cat.}{}^{-1}$ were achieved for $Co_2B$ (1 : 8) variant at −0.3 V *vs.* RHE with a high TOF value of 0.74 $h^{-1}$.

 

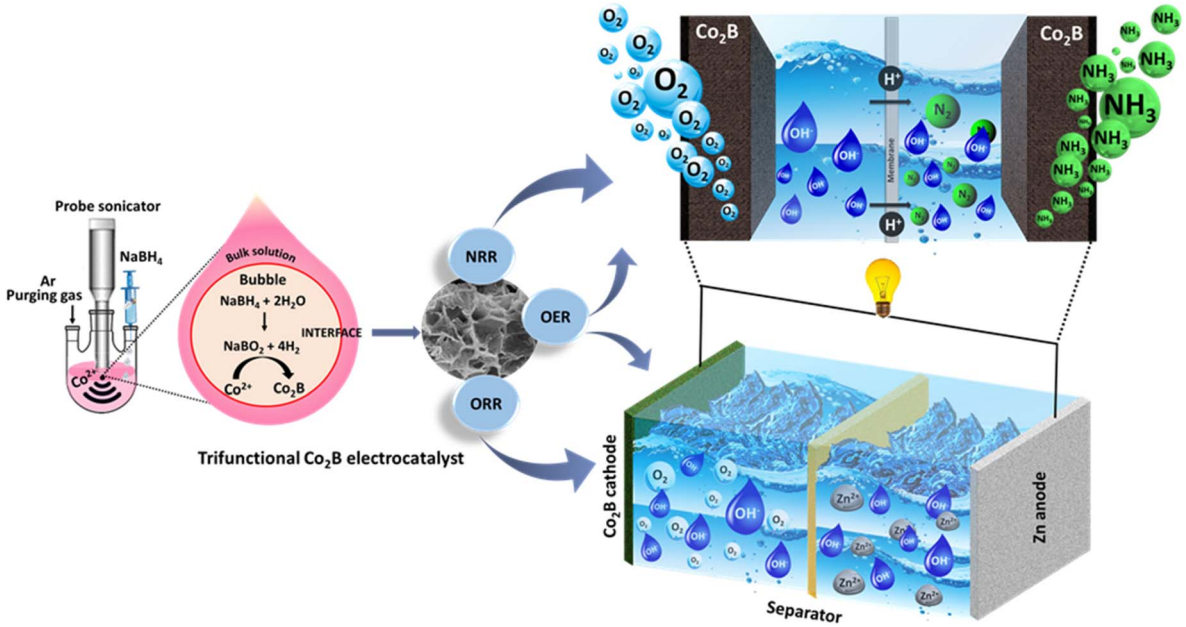


Scheme 1 Schematic representation of the controlled sonochemical synthesis of cobalt boride catalysts signifying trifunctional activity towards NRR/ORR/OER for application in electrochemical ammonia production by as-assembled batteries.

When compared with the recently reported literature in alkaline media, the $Co_2B$ catalyst in this study outperforms in terms of F.E. and $NH_3$ production yield rate (Table S1A, ESI†). The presence of a peak related to NH stretching (1455 $cm^{-1}$) in the FT-IR spectra designates the formation of $NH_3$ after NRR (Fig. S5B, ESI†).[72] More interestingly, Nessler's test data acquired for $NH_3$ standard solutions (Fig. S5C, ESI†) and electrolyte samples collected after NRR by $Co_2B$ (1 : 8) for 2 h, validate the $NH_3$ production, in which both of the quantifications methods, *i.e.* indophenol blue and Nessler's reagent methods produced $NH_3$ yields in the order of 2.98 and 2.35 mg $h^{-1}$ $mg_{cat.}^{-1}$, respectively, as presented in Table S1B (ESI).† However, $Co_2B$ (1 : 4) and $Co_2B$ (1 : 12) showed F.E. of 9.03% and 5.86% with $NH_3$ yield rates of 844.78 μg $h^{-1}$ $mg_{cat.}^{-1}$ and 363.72

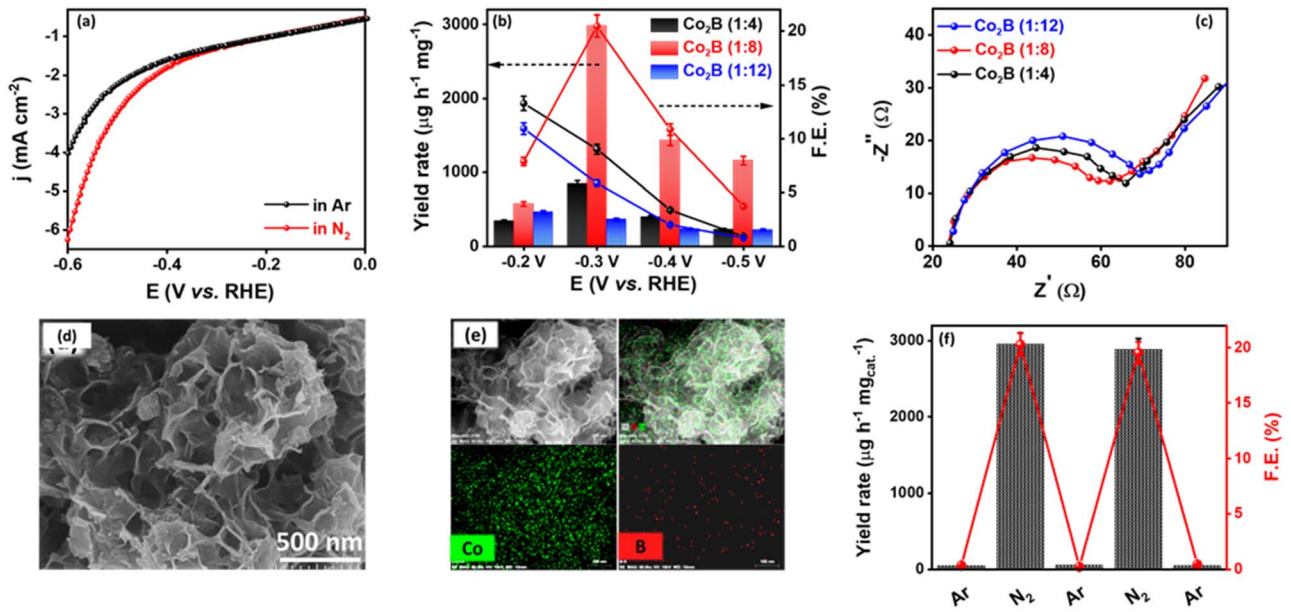


Fig. 1 (a) Linear sweep voltammograms for $Co_2B$ (1 : 8) in Ar- and $N_2$-saturated 0.1 M KOH, (b) comparison of yield rates and F.E. of $Co_2B$ catalysts at different applied potentials, (c) Nyquist plots, (d) FE-SEM image of $Co_2B$ (1 : 8) and (e) corresponding elemental dot mapping showing uniform distribution of Co and B elements over the scanned area. (f) F.E. and yield rates obtained during NRR under switching gas-feed ($Ar/N_2$) environments.

μg $h^{-1}$ $mg_{cat.}^{-1}$, respectively (Fig. 1b). It is noteworthy to mention that no hydrazine was detected during NRR when tested by applying the Watt–Chrisp method (Fig. S6, ESI†), revealing the selectivity of the catalyst for $NH_3$ production. The superior activity of $Co_2B$ (1 : 8) towards NRR could be attributed to the facile kinetics of the interfacial charge transfer process, which is in turn related to the electron transfer at the electrode–electrolyte interface caused by the change in the electronic structure of the catalyst material due to a strong M–B bond to enhance NRR (explained in detail in the subsequent section).[59] This was evidenced by electrochemical impedance spectroscopic (EIS) studies. As expected, the $Co_2B$ (1 : 8) composite revealed the lowest charge transfer resistance ($R_{ct}$) of 35.85 Ω shown by the semicircle behavior compared to the other two variants following the order $Co_2B$ (1 : 8) < $Co_2B$ (1 : 4) < $Co_2B$ (1 : 12) (Fig. 1c and Table S2A, ESI†). The lower $R_{ct}$ of $Co_2B$ (1 : 8) signifies the dominance of faster kinetics towards e-NRR due to higher conductivity and facilitated electron transport at the electrode–electrolyte interface. This facile kinetics could be due to the exposure of higher numbers of electroactive sites than the other variants *viz.*, $Co_2B$ (1 : 4) and $Co_2B$ (1 : 12). This was supported by electrochemical surface area (ECSA) evaluated by double layer capacitance in the non-faradaic region in which $Co_2B$ (1 : 8) showed the highest $C_{dl}$ of 420 μF and ECSA of 10.5 $cm^2$, respectively, followed by $Co_2B$ (1 : 4) and $Co_2B$ (1 : 12) (Fig. S7 and Table S2B, ESI†). The higher surface area of $Co_2B$ (1 : 8) originates from both the inter-sheet space and intra-sheet holes, thus resulting in slit-shaped porosity. This is supported by field emission scanning electron microscopic (FE-SEM) images (Fig. 1d). However, $Co_2B$ (1 : 4) and $Co_2B$ (1 : 12) show variation in morphological features, in which spherical nanoparticles were observed for $Co_2B$ (1 : 12) with an increase in boron content, and stacks of assembled nano-particles were observed for $Co_2B$ (1 : 4) depicted in Fig. S8A;† further increase in boron content ($Co_2B$ (1 : 8)) resulted in surface nanostructuring, thus forming porous nanosheets. The elemental dot mappings of $Co_2B$ (1 : 8) porous nanosheets show a uniform distribution of the respective elements Co and B over the scanned area, as illustrated in Fig. 1e.

More interestingly, the BET surface area measurements were carried out for all the catalysts to determine the pore size and surface area values. The $N_2$ adsorption–desorption isotherms of $Co_2B$ catalysts represent a type IV curve with a hysteresis loop, indicating the mesoporous nature of all the designed catalysts. $Co_2B$ (1 : 8) catalyst possesses a large surface area of 103 $m^2$ $g^{-1}$, which is higher than that of the BET surface area obtained for the $Co_2B$ (1 : 4) catalyst. On further increasing the $NaBH_4$ concentration in the $Co_2B$ (1 : 12) catalyst, the overall surface area of the composite decreased. Thus, the active sites for reactant adsorption over the $Co_2B$ (1 : 8) catalyst were provided by its high surface area (Fig. S8B and Table S2C, ESI†).

The synthesized porous $Co_2B$ (1 : 8) nanosheets are highly hydrophobic compared to other variants due to the 'lotus effect' resulting in surface nanostructuring, which influences the electrocatalytic activity of the catalyst towards NRR.[73] It is clear from the water contact angle measurements that $Co_2B$ (1 : 8) exhibits a higher surface hydrophobicity with a contact angle of 115°, which is higher than other variants *viz.* $Co_2B$ (1 : 4), $Co_2B$ (1 : 12) with a contact angle of 105° and 96.5° respectively (Fig. S8C, ESI†). Thus, the increased surface hydrophobicity of the $Co_2B$ (1 : 8) catalyst can effectively decrease the rate of accessibility of $H_2O$ molecules ($H^+$ donor) to the catalyst, resulting in the obstruction of HER. This demonstrates the remarkable activity of $Co_2B$ (1 : 8) towards NRR owing to suppressed HER at the cathode. To substantiate HER suppression by the catalyst, we performed chronoamperometry under Ar and $N_2$ saturated 0.1 M KOH subsequently by switching the gas feed from Ar to $N_2$ and *vice versa* after every 2 h. A rapid increase in cathodic current density was observed when the gas feed is switched from Ar to $N_2$, whereas a decrease was observed when the gas feed is switched back to Ar from $N_2$ (Fig. S9, ESI†). This is evident in the catalyst's ability to suppress HER in the presence of $N_2$ and the high stability of the catalyst during electrolysis. Upon the quantification of the samples collected after the experiment, a rapid increase in both yield and F.E. is observed when the Ar gas stream is changed to $N_2$. However, on switching back to Ar, no $NH_3$ production was observed, indicating inactivity towards NRR in the absence of an $N_2$ atmosphere (Fig. 1f, S9 and S10, ESI†), which implies that the source of nitrogen in the $NH_3$ production is externally purged $N_2$ only. This was further supported by chronoamperometry measurements at open circuit potential (OCP), in which no $NH_3$ production exists in the presence of Ar after chronoamperometry at −0.3 V, indicating that only the $N_2$ purged into the electrolyte contributes to the $NH_3$ production (Fig. S10, ESI†). Notably, any nitrate/nitrite species in the electrolyte, which may add to the false estimation of $NH_3$ yield, are found to be absent as well (Fig. S11, ESI†).[74]

Another potential source of contamination during NRR is the presence of NO, $NO_2$, and $N_2O$ in the gas supplies used and needs to be detected, quantified and subsequently eliminated to avoid any overestimation of $NH_3$ yield. To serve this purpose, we followed a rigorous protocol in which $NO_x$ concentration in gas supplies was traced and quantified before NRR.[75] First, the concentration of $N_2O$ if any in the gas supplies *viz.* $^{14}N_2$, $^{15}N_2$ and Ar were quantified using GC-MS,[76] from which a total of 0.06 ppm and 0.07 ppm $N_2O$ contamination was detected, while the $N_2O$ was below the detection limit (below 0.01 ppm) for Ar gas supply (Fig. S12A, ESI†). Other impurities, including trace $NO/NO_2$ and $NH_4^+$, were quantified by employing the colorimetric method, which yielded a total of 0.09 and 0.08 ppm $NH_4^+$ in $^{14}N_2$ and $^{15}N_2$ gas-feed but no $NH_4^+$ in Ar gas-supply when trapped in acid solution. Note that 0.6 ppm, 1.1 ppm and 1.2 ppm of $NO_x$ were estimated for Ar, $^{14}N_2$ and $^{15}N_2$ gas supplies, respectively (Fig. S12B, ESI†). Even this small amount of contamination could impose a huge overestimation of $NH_3$ yield because $NO_x$ may undergo a reduction reaction under identical experimental conditions and potential ranges. Therefore, after tracing all these possibilities of interference by $NO_x$ contamination during NRR, the same was then eliminated by carrying out gas purification by $KMnO_4$ trap and $H_2SO_4$ solution (scrubbing solution) prior to every NRR measurement in this study. Additionally, to confirm the possible elimination of the $NO_x$ contaminants, we again quantified the same gaseous

 

samples after purification by applying GC-MS and colorimetric methods (Fig. S13, ESI†). The absence of $NO_x$ and $NH_4^+$ impurities by both procedures is evident in the true estimation of $NH_3$ yield in this study. For better understanding, a distinct comparison of $NO_x$ contamination in gas supplies before and after the purification is provided in Table S3 (ESI).† Later, the high $NH_3$ yield rate achieved during NRR further prompted us to conduct $^{15}N_2$ isotopic labelling experiments to confirm the true estimation of $NH_3$. After bulk electrolysis for 2 h under a purified $^{15}N_2$ gas supply, the formation of $^{15}NH_4^+$ was evaluated using $^1$H nuclear magnetic resonance (NMR) spectroscopy.

After potential electrolysis by $Co_2B$ (1 : 8) at −0.3 V (*vs.* RHE) for 2 h using Ar, $^{15}N_2$ and $^{14}N_2$ gas supply, the $^1$H NMR spectra for samples under $N_2$ environment match well with standard couplings, revealing that the $NH_3$ produced in this study is indeed from the electroreduction of supplied $N_2$ rather than any possible contaminants (Fig. S14, ESI†). In addition to the qualitative tracing of true $NH_3$ source, it is equally important to quantify the obtained yield rates under both $^{14}N_2$ and $^{15}N_2$ environments. To serve this purpose, we adapted two methods, *i.e.* $^1$H-NMR spectroscopy and liquid chromatography-mass spectroscopy (LC-MS), respectively. The calibration curves were first extracted from the $^1$H-NMR spectrum of the standard aqueous $^{15}NH_4^+$ and $^{14}NH_4^+$ solutions with different concentrations from 1.0 to 5.0 ppm (Fig. S15A, ESI†). The $NH_3$ yield was then quantified for NRR by $Co_2B$ catalyst at different time intervals (1 h and 2 h) performed under both $^{14}N_2$ and $^{15}N_2$ saturated electrolytic conditions (Fig. 2a and b). The $NH_3$ yield rate was calculated to be 1.87 (1 h) and 2.94 mg $h^{-1}$ $mg_{cat.}^{-1}$ (2 h) for $^{14}NH_4^+$ as well as 1.8 mg $h^{-1}$ $mg_{cat.}^{-1}$ (1 h) and 2.92 mg $h^{-1}$ $mg_{cat.}^{-1}$ (2 h) for $^{15}NH_4^+$ produced during NRR, respectively, which are analogous to each other. However, the $NH_3$ yield rate obtained from the indophenol blue method for $^{14}NH_3$ (2.94 mg $h^{-1}$ $mg_{cat.}^{-1}$) and $^{15}NH_3$ (2.93 mg $h^{-1}$ $mg_{cat.}^{-1}$) also complements each other. In the end, LC-MS was employed to validate the $NH_3$ yield after the isotope labelling experiment, which yields overall ammonia production yield rates of 2.98 and 2.95 mg $h^{-1}$ $mg_{cat.}^{-1}$ for NRR performed under $^{14}N_2$- and $^{15}N_2$-saturated electrolyte conditions, respectively (Fig. S15B, ESI†). Fig. 2c and Table S4 (ESI)† demonstrate the comparison of $NH_3$ yield obtained after isotope labelling experiments *via* various methods.

The disparity in the NRR activity of the catalysts with only a difference in metal : boron ratio during synthesis was then scrutinized by performing a series of *ex situ* characterizations. The P-XRD pattern of $Co_2B$ (1 : 8) in Fig. S16A (ESI)† reveals the formation of $Co_2B$ with a distinct peak at $2\theta = 45°$ with no other peaks, indicating that the formation of pure amorphous $Co_2B$ phase agrees with that of the literature.[77] The presence of additional peaks at 26° and 36.8° related to $B_2O_3$ (JCPDF card: 06-0297) and elemental B (JCPDF card: 12-0377) imply the amorphous boron-oxide layer over the catalyst surface in $Co_2B$ (1 : 12). However, we cannot deny the fact that the high intensity peak for $Co_2B$ can suppress the peaks for metallic cobalt and $Co(OH)_2$ phase in XRD patterns. Therefore, to check the purity of the $Co_2B$ catalyst prepared, we further performed Raman spectroscopy analysis. As shown in Fig. S16B (ESI),† the Raman spectra for $Co_2B$ (1 : 4) and $Co_2B$ (1 : 8) do not reveal any peak related to metallic cobalt or $Co(OH)_2$ phase, while the Raman spectra of $Co_2B$ (1 : 12) show the bands corresponding to $B_2O_3$ at 650 and 950 $cm^{-1}$, respectively, along with a low intensity band at 465 $cm^{-1}$ related to the O–Co–O bond in $Co(OH)_2$. These results show that the bulk phase in the $Co_2B$ (1 : 8) catalyst is $Co_2B$ only, and upon further increasing the amount of boron, the catalyst forms a composite of $Co_2B/B_2O_3/Co(OH)_2$ with a major phase as $Co_2B$ only.

The nanosheet structure of $Co_2B$ (1 : 8) is supported by transmission electron microscopy (TEM) images (Fig. 3a and b). The high resolution-TEM (HR-TEM) images in Fig. 3c show the edge site of entangled nanosheets; these images do not show any clear lattice fringes but a very short-range ordered atomic arrangement at a few locations with an interlayer *d* spacing of 0.2 nm corresponding to the (210) plane of $Co_2B$ (Fig. 3d and e), and these arrangements could be embedded within the diffused amorphous phase,[78,79] which are consistent with XRD data.[77] The energy dispersive spectroscopic (EDS) elemental dot mapping reveals the co-existence of Co, B, and O elements, which are uniformly distributed in the scanned area, and their compositions are presented in Table S4 (Fig. S17, ESI).† The ratio of Co : B in $Co_2B$ (1 : 8) was estimated from the atomic percentage obtained from EDS (Table S5, ESI†) and was found to be 1.83 : 1 with a product comprising B (26.07 at%) and Co (47.76 at%) and the others mostly oxygen, yielding an

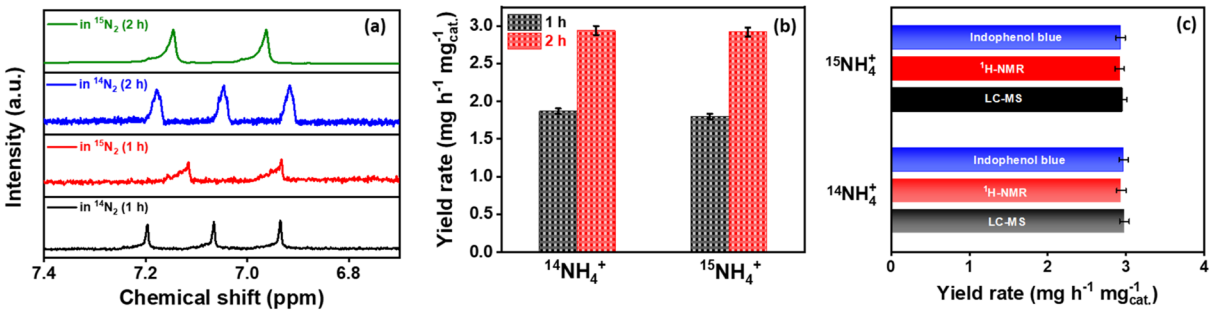


Fig. 2 (a) $^1$H-NMR spectrum acquired after NRR isotope labelling experiments using $Co_2B$ (1 : 8) catalyst for different time intervals and (b) corresponding yield rates calculated from the same. (c) Bar diagram comparison of $^{14}NH_4^+$ and $^{15}NH_4^+$ yield rates obtained using different quantification methods.

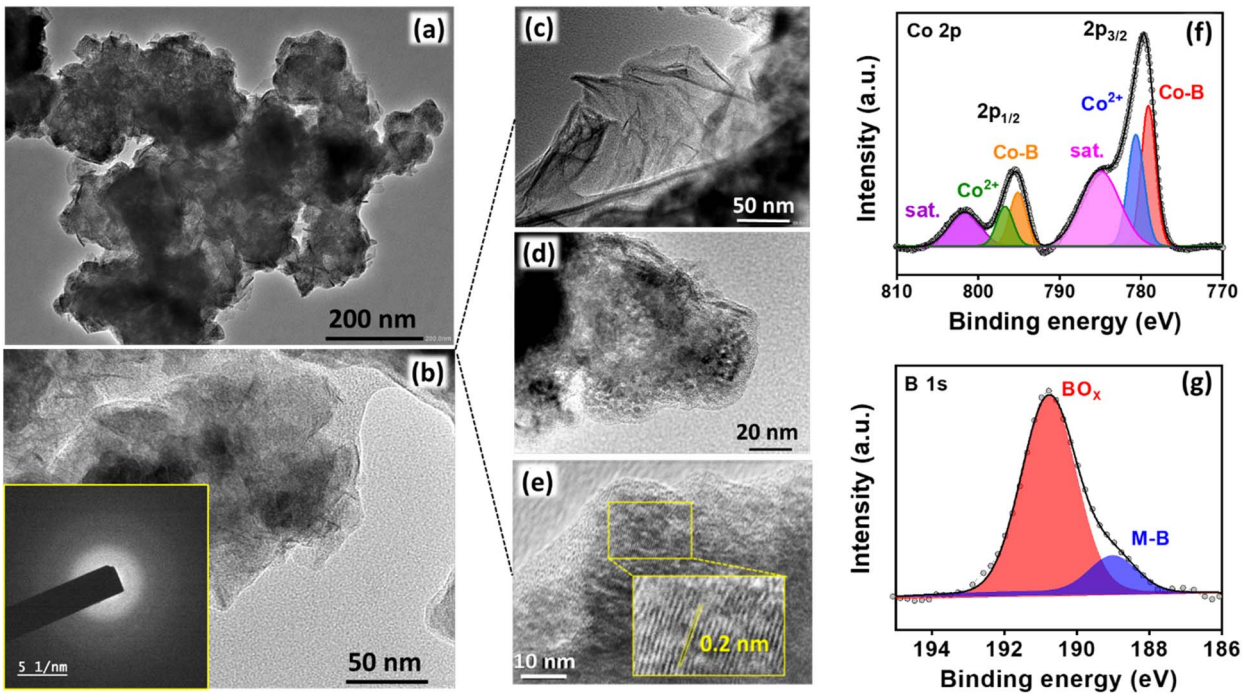


Fig. 3 (a–e) HR-TEM images of $Co_2B$ (1 : 8) at different magnifications (inset of (b) shows SAED pattern for $Co_2B$ (1 : 8) revealing an amorphous nature and inset of (e) shows *d*-spacing corresponding to $Co_2B$ with short range atomic arrangement at few locations). (f) Deconvoluted XP spectra of Co 2p and (g) XP spectra of B 1s for $Co_2B$ (1 : 8) catalyst.

approximate atomic Co : B ratio of 2 : 1. From XPS, the ratio of Co : B was observed to be 2.3 : 1, yielding the final composition of $Co_{2.3}B_{1.0} \approx Co_2B$. Moreover, the MP-AES analysis produces a total of 79.1% cobalt and 10.5% boron in the catalyst, which describes the presence of $Co_2B$ as a major phase in the proposed catalyst with minute impurities.

Subsequently, to understand the surface properties of Co and B in the $Co_2B$ (1 : 8) catalyst, X-ray photoelectron spectroscopy (XPS) analysis was performed. The XP survey spectrum indicates the presence of both Co 2p and B 1s peaks (Fig. S18, ESI†) with no additional peaks due to impurity, which reinforces the fact that the synthesized catalyst is highly pure.

The deconvoluted Co 2p XP spectra in Fig. 3f display two distinct peaks at binding energies of 779.07 and 795.4 eV with additional satellite peaks at 785.1 eV and 801.7 eV corresponding to Co $2p_{3/2}$ and Co $2p_{1/2}$, respectively. The presence of a peak at 778.5 and 795 eV is attributed to the formation of metal-boride.[80] However, B 1s XP spectra were deconvoluted into two peaks in which the peak at 188.6 eV corresponds to the interaction of boron with cobalt, which is shifted towards higher energies by 1.6 eV w.r.t elementary boron (187 eV) most probably due to electron transfer from B to vacant d-orbital of Co metal.[81] Moreover, an additional dominant peak at 191.5 is due to boron-oxo species (Fig. 3g), which is characteristic of amorphous metal-borides upon exposure to the atmosphere. The reason behind the large B–O peak in the B 1s XP spectrum is the presence of oxidized boron species at a binding energy value of 191.5 eV. This indicates that the $Co_2B$ nanoparticles were oxidized to a certain degree, while the bulk phase remains in the $Co_2B$ state. The formation of boron oxide was quite expected as the work-up (filtering and washing) of the prepared catalyst was performed in the air. This $BO_2^-$ species might have appeared because of the self-hydrolysis of the non-stabilized $NaBH_4$. The commercial bulk $Co_xB$ sample also shows the peaks related to boride and borate/oxidized boron.[64,80] Moreover, the activity and stability of the catalyst during NRR are crucial, for which a stability test was conducted by applying chronoamperometry at −0.3 V for 10 h. Fig. S19 (ESI)† illustrates a stable current density response, and the quantification of $NH_3$ after every 2 h reveals a negligible change in both faradaic efficiency and $NH_3$ yield rate (Fig. 4a), assisting the high stability of electrocatalyst. Moreover, to observe the structural stability of the catalyst after NRR, we examined its physicochemical properties by P-XRD, FE-SEM and EDS dot mapping. The morphology was retained after the 10 h of NRR stability test, with well-distributed boron and cobalt over the entire scanned area in EDS dot mapping analysis, as shown in Fig. S20 (ESI).† All these findings demonstrate the high durability of $Co_2B$ for electrochemical $NH_3$ production.

## Theoretical investigations

To gain a deep insight into the NRR mechanism over the $Co_2B$ surface, systematic electronic structure calculations along with the framework of density functional theory (DFT) formalism were performed to anticipate the nitrogen reduction to ammonia on the experimentally synthesized $Co_2B$ catalyst surface. Because no hydrazine formation was witnessed during the quantification of products after NRR, we determined the

 

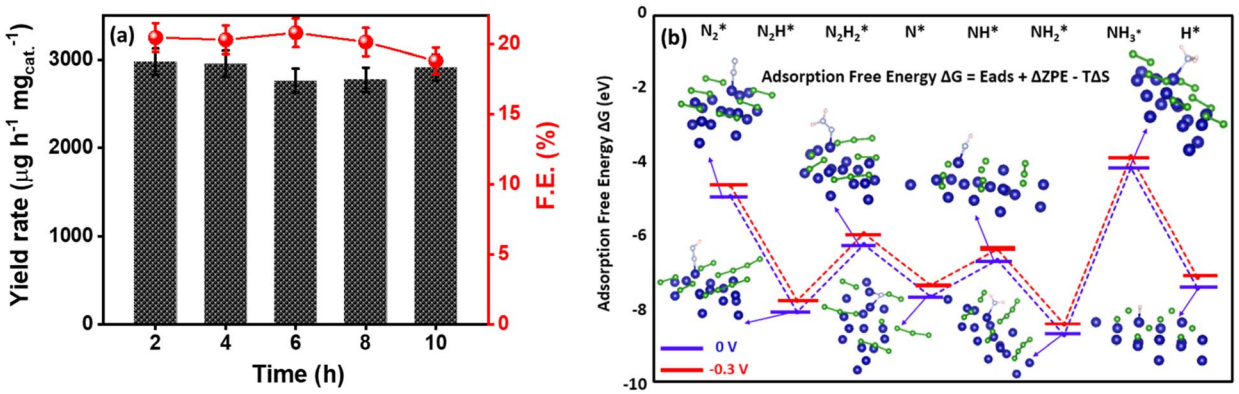


Fig. 4 (a) F.E. and $NH_3$ yield obtained after chronoamperometry tests performed for 10 h under $N_2$-saturated 0.1 M KOH for $Co_2B$ (1 : 8). (b) Free energy diagrams of the NRR distal pathway on $Co_2B$ surface (Co active site) at applied potentials of 0 and −0.3 V and $H^+$ adsorption at identical potentials.

adsorption free energies for seven intermediates ($N_2^*$, $N_2H^*$, $N_2H_2^*$, $N^*$, $NH^*$, $NH_2^*$, and $NH_3^*$) corresponding to both the Co (Fig. 4b) and B sites (Fig. S21, ESI†) of the catalytic $Co_2B$ surface. It seems that the Co site is more favorable for the NRR. The greater electron affinity of Co could be a possible reason for the favorable NRR mechanism. We also calculated the adsorption free energy of hydrogen (H*) to check the possibility of a hydrogen evolution reaction. In the plot reaction, coordinates were generated from Gibbs adsorption free energy ($\Delta G$) corresponding to different electrode potentials of 0 V and −0.3 V (Table S5B and C, ESI,† where the maximum $NH_3$ F.E. is achieved). Here, the adsorption energy is defined as follows:

$$E_{ad} = E_{sub+ads} - E_{sub} - E_{ads},$$

where $E_{sub+ads}$ is the total energy of the optimized structure, $E_{sub}$ is the energy of the catalyst, and $E_{ads}$ is the energy of the adsorbate. Gibbs free energy can be determined as follows:

$$\Delta G = E_{ad} + \Delta ZPE - T\Delta S + \Delta G_U,$$

where $E_{ad}$ is the adsorption energy of intermediates, ΔZPE is the difference in the zero point energy between the adsorbed state and gas phase, $T\Delta S$ is the entropic contribution, and $\Delta G_U$ is the free energy contribution related to the applied external potential. Fig. 4b demonstrates the free energy plot for NRR at the $Co_2B$ surface (Co active site) at different applied potentials of 0 and −0.3 V *vs.* RHE. Under thermoneutral conditions ($\Delta G \sim$ 0.0 eV), the catalyst with an adsorption free energy value close to zero possesses a facilitated reaction rate due to a lowered activation barrier. In this scenario, the $\Delta G_{N_2^*}$ value over the $Co_2B$ surface is −4.93 eV at 0 V of the applied potential, which supports the high activity of the catalyst at −0.3 V (with a $\Delta G_{N_2^*} = -4.63$ eV). Further NRR mechanism analysis was performed by the free energy diagram, in which the first step proceeds *via* end-on adsorption of $N_2$ molecule over the Co active site of the $Co_2B$ surface with an adsorption energy of −4.63 eV at −0.3 V (*vs.* RHE). Thereafter, the adsorbed $N_2$ ($N_2^*$) species undergoes the first hydrogenation step ($H^+/e^-$) to form $N_2H^*$ with a downhill in the corresponding free energy profile by −7.74 eV. In the second hydrogenation step, the $N_2H^*$ intermediate captures another $H^+ + e^-$ pair to form $N_2H_2^*$ with an uphill Gibbs free energy change of 1.81 eV (rate-limiting step). The third hydrogenation step proceeds with the formation of $N^* + NH_3$, leading to the release of the first $NH_3$ molecule by following an exothermic pathway with a free energy change of −1.39 eV. Successful hydrogenation of the remaining adsorbed N (N*) occurs with corresponding free energy changes of 0.98, −2.03 and 4.51 eV to form NH*, $NH_2^*$ and $NH_3^*$, respectively, followed by the desorption of the second $NH_3$ molecule.

In addition to the activity of the catalyst for the adsorption and activation of the N≡N bond, selectivity over $H^+$ adsorption to suppress competing HER is an imperative aspect. Under thermoneutral conditions, the optimal catalysts should not attain an adsorption free energy close to zero for $H^+$ adsorption. The value of adsorption free energy corresponding to $N_2$ is calculated to be −4.63 eV at −0.3 V, while it is −7.12 eV for $H^+$ adsorption. This supports the fact that the $Co_2B$ catalyst surface provides optimum active sites for NRR than HER at an identical potential.

### Oxygen bifunctional activity for the air-cathode

We further investigated the potential efficacy of $Co_2B$ variants in oxygen bifunctional activity *viz.* the oxygen reduction reaction (ORR) and oxygen evolution reaction (OER) to understand its ability to serve as an air cathode in Zn–air batteries. Initially, the catalytic activity of the $Co_2B$ catalyst towards ORR was examined in a 0.1 M KOH electrolyte. The cyclic voltammetry (CV) curves of $Co_2B$ (1 : 8) exhibit the most positive reduction peak potential at 0.97 V *vs.* RHE (Fig. 5a and S22, ESI†), indicating its superior ORR activity compared with those of $Co_2B$ (1 : 4) and $Co_2B$ (1 : 12). As observed from voltammetric curves in Fig. 5a, the $Co_2B$ (1 : 8) shows an obvious increase in cathodic current at a potential of 0.97 V *vs.* RHE in an $O_2$ saturated 0.1 M KOH electrolyte, and no such behaviour was observed in an oxygen free electrolyte ($N_2$ saturated). The obtained reduction potential is more positive compared to those of the other two variants. These results can be attributed to a reduction in oxygen. To

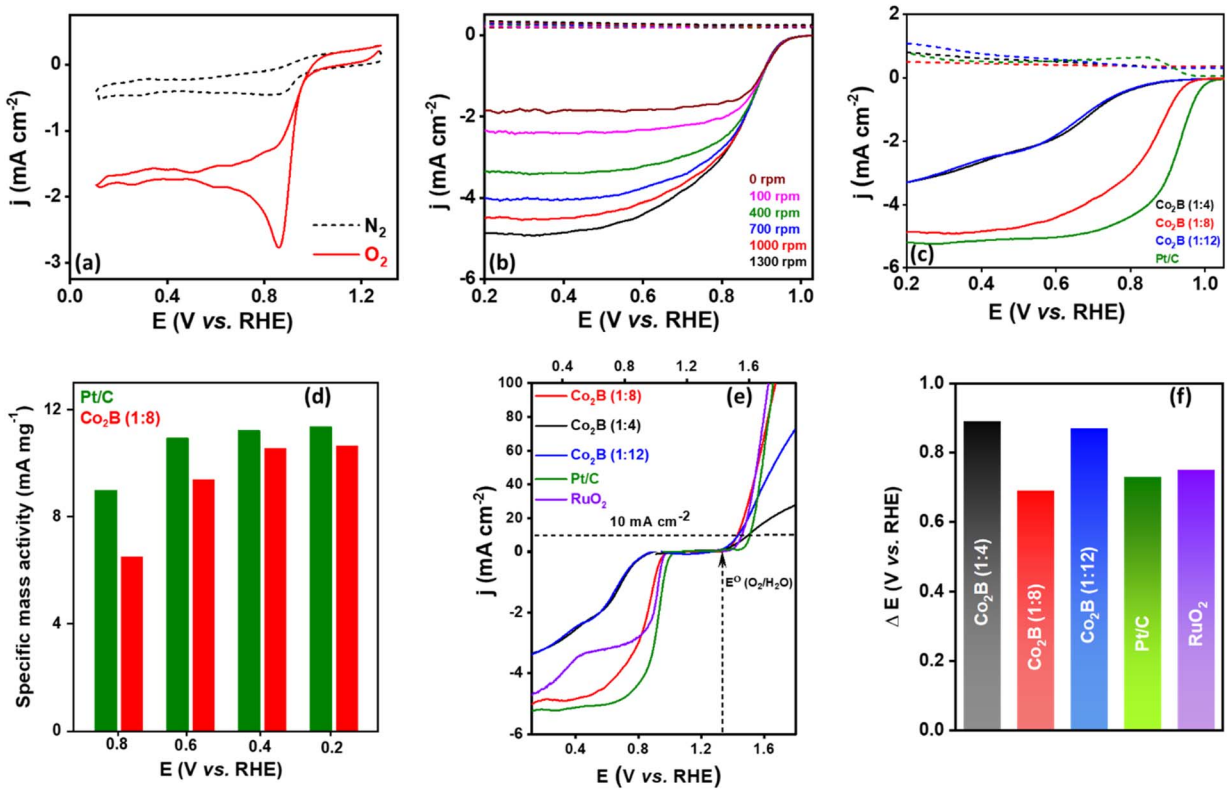


Fig. 5 (a) Cyclic voltammogram of $Co_2B$ (1 : 8) for oxygen reduction activity in 0.1 M KOH at 25 mV $s^{-1}$. (b) RRDE polarization curves of $Co_2B$ (1 : 8) in the presence of $O_2$ at varying rotation rates and at a scan rate of 5 mV $s^{-1}$. (c) Comparison of RRDE curves of $Co_2B$ catalysts with state-of-art Pt/C catalyst. (d) Comparison of specific mass activity for Pt/C and $Co_2B$ (1 : 8) at different potentials, (e) oxygen bifunctional activity of $Co_2B$ catalysts and commercial benchmark catalysts and (f) comparison of a potential gap for Zn–air battery.

understand the kinetics of the ORR, rotating ring disc electrode measurements (RRDE) were performed at various rotating rates under hydrodynamic conditions in 0.1 M KOH electrolyte (Fig. S23, ESI†). The RRDE curves depicted in Fig. 5b disclose an exponential current increment for $Co_2B$ (1 : 8) with an increase in rotation rate and reached up to the diffusion-limited current density of $-4.9$ mA $cm^{-2}$ at 1300 rpm with an onset potential ($E_{onset}$) of 0.98 V *vs.* RHE (Table S6A, ESI†). The comparative analysis of disc and ring current densities depicted in Fig. 5c indicates that $Co_2B$ (1 : 8) has activity superior activity compared to other variants. Notably, the ring current of $Co_2B$ (1 : 8) is lower than those of the other variants. The half wave potentials can be a descriptor of ORR activity in the mixed kinetic/diffusion-controlled region, wherein $Co_2B$ (1 : 8) exhibits a half-wave potential ($E_{1/2}$) of 0.83 V, which is 170 and 140 mV higher than that of $Co_2B$ (1 : 12) and $Co_2B$ (1 : 4) respectively, suggesting superior ORR activity. More interestingly, compared with the benchmark catalyst, *i.e.* Pt/C, a comparable activity is observed in terms of onset potential and diffusion limiting current density and specific mass activity at a similar potential (Fig. 5c, d and S24, ESI†). Hence, apart from the remarkable NRR activity, $Co_2B$ (1 : 8) exhibits outstanding ORR activity. The kinetic parameters were evaluated using Koutecky–Levich (K–L) plots derived from LSV curves to gain deeper insights into the mechanism governing the ORR reaction. The K–L plots represent a linear behavior between $j^{-1}$ *vs.* $\omega^{-1/2}$ attributed to first-order reaction kinetics with respect to the dissolved $O_2$ (Fig. S25, ESI†).

Further, an apparent $4e^-$ pathway, followed by $Co_2B$ (1 : 8) during oxygen reduction, was confirmed by calculating the number of $e^-$ transfer ($n$) from RRDE curves, and the quantitative estimation of peroxide (Fig. S26 and Table S6B, ESI†) produced during ORR was obtained using the following equations:

$$n = 4I_d/[I_d + (I_r/N)], \quad (1)$$

$$\%\ H_2O_2 = 200 \times (I_r/N)/[I_d + (I_r/N)]. \quad (2)$$

Here, $I_d$ denotes the disk current and $I_r$ denotes the ring current, and $N$ denotes the collection efficiency of the ring, which was taken to be 0.36 in this study. The bar diagram in Fig. S27 (ESI)† depicts the amount of $H_2O_2$ and the number of electrons transferred during ORR for all the catalytic variants. $Co_2B$ (1 : 8) impersonates a complete four electron transfer ($n \approx 4$), revealing its ability to conduct the direct $4e^-$ pathway during $O_2$ reduction to $H_2O$ as a final product. Additionally, the yield of $H_2O_2$ generated was found to be very low (less than 9%) for $Co_2B$ (1 : 8), which is highly anticipated, because $H_2O_2$ production could adversely affect the cell components.[82] Therefore, chronoamperometry, performed at an onset potential of ORR for a time duration of 1 day in $O_2$-saturated 0.1 M KOH, showed

 

a stable current response even after a prolonged stability study (Fig. S28, ESI†). These outcomes clearly validate the capability of $Co_2B$ (1 : 8) to reduce $O_2$ with enhanced activity and stability, which is very essential for practical applications. To determine the electrocatalytic ability of the $Co_2B$ catalysts towards the OER, linear sweep voltammetry (LSV) experiments were performed in 0.1 KOH at a scan rate of 5 mV $s^{-1}$. Analogous to the activity obtained during ORR, $Co_2B$ (1 : 8) displays significantly enhanced OER activity than $Co_2B$ (1 : 4) and $Co_2B$ (1 : 12) under identical conditions. It is evident from Fig. S29 (ESI)† that oxygen gas evolution was observed at 1.5 V on the surface of $Co_2B$ (1 : 8) and became sturdy as the potential scan progressed towards anodic potentials, reaching 100 mA $cm^{-2}$ at 1.6 V. The $Co_2B$ (1 : 8) achieves a 10 mA $cm^{-2}$ current density at an overpotential of ($\eta$) 290 mV, which is lower than that of $Co_2B$ (1 : 4) and $Co_2B$ (1 : 12) with an $\eta$ value of 360 and 300 mV, respectively (Table S7, ESI†).

Hence, apart from the superior ORR activity, $Co_2B$ (1 : 8) also shows remarkable OER activity. The higher OER activity could be attributed to the strain originating in $Co_2B$ due to the chemical hybridization of B 2p and Co vacant 3d orbitals, which may presumably reduce the activation energy barrier for Co oxidation.[57] This strong hybridization is supported by the presence of the M–B bond revealed by XPS studies (Fig. 3g), which could facilitate the OOH* intermediate formation and in turn OER (M–OH/M–OOH species being an active site). The Tafel slope of the $Co_2B$ (1 : 8) supports facilitated OER, which was found to be the least when compared with other catalysts, indicating the faster reaction rate during OER (Fig. S30, ESI†). The chronopotentiometric stability test of $Co_2B$ (1 : 8) shows a negligible change in the overpotential required to deliver 10 mA $cm^{-2}$ even over 24 h (Fig. S31a, ESI†). In addition, the stability was further examined under different current densities from 10 to 50 mA $cm^{-2}$, in which a continuous increase in cell potential was observed as the current density increased but underwent rapid stabilization (Fig. S31b, ESI†). The cell potential was again restored when the applied current density returns to 10 from 50 mA $cm^{-2}$, indicating superior stability.

Metal borides are usually susceptible to undergo *in situ* electrochemical oxidation during OER to generate metal oxyhydroxides and metal borates.[83] The post-OER XPS analysis acquired (Fig. S32, ESI†) after 24 h stability test reveals the formation of Co–OOH species at 779.1 eV in Co 2p XP spectra. The deconvoluted B 1s XP spectra show a peak related to boron-oxo species (B–O), but the diminished intensity of the B peak related to boride could be attributed to the shielding of the catalyst surface by the oxyhydroxide layer after the OER. This B–O species may either stick onto the catalyst surface or dissolve in the electrolyte and further create pores to increase active sites during OER.[57] During OER in alkaline electrolytes, either Co–OOH or B–O species could serve as an active site. In one case, Co–OOH may serve as the major active site, while borate may modulate the adsorption energies of the reaction intermediates. The other case could be the improved electron transfer between partially oxidized metal oxyhydroxide and the current collector due to active non-oxidized metal boride centers.[84] Therefore, the overall significant electrocatalytic activity of $Co_2B$ (1 : 8) indicates that it is an extremely capable bifunctional oxygen catalyst. This is further validated by the oxygen polarization curves representing ORR and OER bifunctional activity (Fig. 5e). An exclusive factor to investigate the ability of different catalysts towards oxygen bifunctional activity is the potential gap ($\Delta E$). In this study, the $\Delta E$ ($\Delta E = E_{@10\ mA\ cm^{-2}} - E_{1/2@ORR}$) value was calculated using the potential values amid OER (10 mA $cm^{-2}$) and ORR (half-wave potential). The lower $\Delta E$ value of 0.69 V for $Co_2B$ (1 : 8) considerably demonstrates the superior electrocatalytic performance for ORR/OER than 0.89 V for (1 : 4) and 0.87 V for the (1 : 12) ratio of $Co_2B$, 0.73 V for Pt/C and 0.75 V for $RuO_2$ (Fig. 5f and Table S8, ESI†). A Zn–air battery equipped with a $Co_2B$ (1 : 8) air cathode was used. To investigate the potential application of the outstanding oxygen bifunctional $Co_2B$ (1 : 8) catalyst towards energy conversion and storage devices, a homemade Zn–air battery was assembled by employing $Co_2B$ (1 : 8) air-cathode catalyst with Zn foil anode using a 6 M KOH + 0.2 M zinc acetate electrolyte. The assembled battery exhibits a high open circuit voltage of 1.45 V (Fig. 6a), which is close to that of Pt/C + $RuO_2$ air cathode (1.48 V) with identical mass loading (2 mg $cm^{-2}$). The polarization curves during discharge and the corresponding power density plots are presented in Fig. 6b and c, respectively. By employing $Co_2B$ (1 : 8) as an air cathode, the peak power density of the battery was found to be 500 mW $cm^{-2}$, which is superior to that of Pt/C + $RuO_2$ (200 mW $cm^{-2}$, Fig. 6c) and those reported in the literature. The high-power density of the battery mainly depends on the discharge efficacy of the catalyst at the cathode, *i.e.* to carry out ORR with high activity in which the high $O_2$ diffusion rate at the cathode is responsible for high discharge current density and thus the high power density. Therefore, in this case, the high peak power density can be related to the following properties.

**High diffusion-limited current density.** This is the diffusion-limited current density that determines the maximum power density. From the discharge polarization curves, we can see a high diffusion-limited current density of 620 mA $cm^{-2}$, resulting in a high power density of 500 mW $cm^{-2}$.

**Low potential gap.** The power density of the Zn–air battery is also affected by the low charge and discharge overpotentials at the air cathode during OER and ORR, respectively. A very low potential gap of 0.61 V is observed in the ZAB employed with the $Co_2B$ air cathode in this case, which results in high power density.

**Positive half-wave potential.** The LSV curves acquired for ORR can be related to the power density of the Zn–air battery, where the half wave potential ($E_{1/2}$) has a strong influence over ohmic losses. A more positive $E_{1/2}$ of the catalyst exhibits tolerance towards the voltage drop of the battery during discharge and thus enhances the power density.

**No corrosion problems at the cathode.** Conventional carbon-based air cathodes suffer from corrosion in alkaline electrolytes at higher oxidation potentials, which leads to poor power and energy density of ZABs. In our case, the air cathode catalyst does not contain carbon and does not undergo deterioration under high oxidative potentials, thus delivering a high power density.

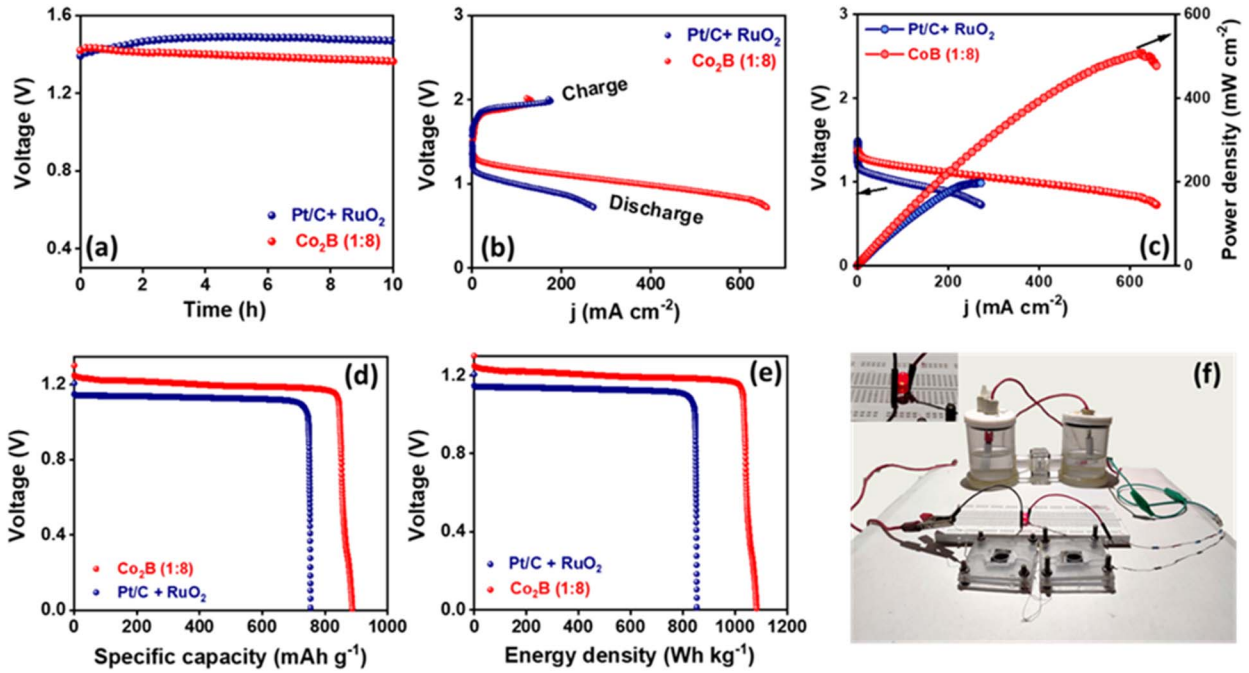


Fig. 6 (a) Open circuit voltage, (b) charge–discharge polarization curves, (c) power density plots extracted from discharge polarization curve for Zn–air battery assembled using $Co_2B$ (1 : 8) and Pt/C as an air cathode. (d) Corresponding specific capacity and (e) energy density curves obtained at 10 mA $cm^{-2}$. (f) Photograph of Zn–air battery-powered NRR full cell setup (air cathode in battery: $Co_2B$ (1 : 8); cathode and anode in NRR full cell: $Co_2B$ (1 : 8)).

More importantly, the $Co_2B$ (1 : 8) air cathode shows a small charge–discharge voltage gap of 0.61 V, which is less than that of Pt/C + $RuO_2$, demonstrating a promising future as an air-cathode alternative to noble metal-based electrodes in Zn–air batteries. $Co_2B$ (1 : 8) air cathode further demonstrates a stable response at 10 mA $cm^{-2}$ with an overall cell voltage of 1.27 V (Fig. 6d and e), resulting in a high specific capacity of 889 mA h $g^{-1}$ and an energy density of 1078 W h $kg^{-1}$, which are higher than those of Pt/C + $RuO_2$ (748 mA h $g^{-1}$ and 860 W h $kg^{-1}$, normalized w.r.t the mass of lost zinc). The durability of the proposed $Co_2B$ (1 : 8) air cathode by galvanostatic-cycling performance of the battery at 10 mA $cm^{-2}$ demonstrates that an initial overall potential gap of 0.61 V is retained to 0.75 V for 17 h, with each cycle having 10 min of discharging and 10 min of charging (Fig. S33A, ESI†). However, Pt/C + $RuO_2$ suffers severe degradation in the potential gap (from 0.63 V to 1.6 V) within 45 cycles (15 h) most probably due to Ostwald ripening and carbon corrosion, leading to the aggregation of noble metals. Further, to validate the practicability of the designed battery, it was connected in series and applied to power an LED. As shown in Fig. S33B (ESI),† two Zn–air batteries equipped with the catalyst provide adequate voltage to power a red LED (2.0 V).

### Zn–air battery-powered NRR

To demonstrate the ability of the assembled Zn–air battery to power the two-electrode NRR cell, we made a setup of two batteries connected in series to supply power to drive ammonia synthesis (Fig. 6f). During the integration of Zn–air batteries (2.9 V) with the full cell $NH_3$ synthesis device, we utilised a resistor (300 Ω) to limit the excessive current supply to the cell, thus maintaining the efficiency of the device to achieve the maximum $NH_3$ production yield rate. A two-electrode NRR cell was constructed by employing $Co_2B$ (1 : 8) as a bifunctional catalyst at both the anode and cathode. The bifunctional ability of the catalyst to carry out NRR at the cathode and OER at the anode is supported using LSV acquired under full cell conditions in a potential ranging from 0 to 2.5 V (Fig. S34, ESI†). The steep increase in current density at 1.6 V describes the onset potential for overall $NH_3$ synthesis. Additionally, LSV was evaluated in Ar and $N_2$ saturated electrolytes to check the ammonia production in full cells using a potentiostat. An increase in current density (cathodic) in the presence of $N_2$ gives a picture of successful nitrogen reduction to ammonia (Fig. S35, ESI†). On further performing 2 h of electrolysis, the home-built NRR cell setup powered by assembled Zn–air batteries could deliver an overall $NH_3$ yield rate of 1048.2 μg $h^{-1}$ $mg_{cat.}^{-1}$ (Fig. S35, ESI†). These results indicate the ability of the catalyst to be applied for practical applications. To date, very few self-powered electrochemical $NH_3$ synthesis setups have been reported, amongst which our study reveals the maximum yield rate within 2 h (Table S9, ESI†). The outstanding trifunctional activity towards NRR/OER/ORR could lead to a new pathway towards the development of cost-effective catalysts for Zn–air battery and $NH_3$ synthesis and their implementation towards powering the ammonia production by sustainable and high-power density rechargeable Zn–air batteries.

 

## Conclusions

In summary, we report the synthesis of cobalt boride ($Co_2B$) catalyst *via* an environment friendly, economical and less-time-consuming sonochemical route using non-expensive precursors. The catalyst demonstrates remarkable activity with a high faradaic efficiency and yield rate for NRR. This high activity is attributed to the strong M–B bond and the nanosheet morphology, providing an ample number of active channels for mass and charge transfer. Systematic DFT investigations are carried out to estimate NRR activity over the $Co_2B$ catalyst surface, in which the Co acts as an active site to adsorb and activate strong N≡N and produce $NH_3$ *via* an associative distal pathway. The undesired products *viz.* $H_2$ owing to the competition between NRR and HER can be effectively suppressed at the catalyst active sites, indicating the high selectivity of $Co_2B$ towards $NH_3$ production. When employed as a cathode catalyst for Zn–air battery, $Co_2B$ (1 : 8) unveils substantial electrocatalytic performance, yielding a reduced potential gap, improved rate of reaction, and high durability. Interestingly, the assembled Zn–air battery can power $NH_3$ synthesis with an appreciable $NH_3$ production yield of 1048.2 μg $h^{-1}$ $mg_{cat.}^{-1}$ after two continuous hours of electrolysis. Being a non-noble, simple and facile synthesis strategy, the high trifunctional activity of $Co_2B$ holds great promise for energy conversion and storage devices.

## Conflicts of interest

There are no conflicts to declare.

## Acknowledgements

D. Gupta thanks DST for DST-INSPIRE fellowship (DST/INSPIRE/03/2017/000005), A. Kafle thanks IIT Ropar for fellowship. T. C. Nagaiah thanks Science and Engineering Research Board (SPG/2021/002415). T. D. and S. C. would like to acknowledge HRI Allahabad and DST-SERB Funding (SRG/2020/001707) for the infrastructure and funding. Computational work for this study was carried out at the cluster computing facility in the Harish-Chandra Research Institute (**https://www.hri.res.in/cluster**). P. P. M. would like to acknowledge INSPIRE PhD Fellowship and IIT Ropar for infrastructure. R. A. also thanks the Swedish Research Council (VR-2016-06014 and VR-2020-04410) for financial support. We are thankful to Sophisticated Analytical Instrumentation Facility (SAIF) and Central Instrumentation Facility (CIL), Panjab University, Chandigarh, India, for providing FE-SEM and HRT-TEM facilities. We also thank LC-MS facility at IIT Ropar procured through FIST-DST grant (SR/FST/CS-I/2018/55) for quantitative product analysis. We acknowledge Prof. Sanjay Mandal and his group at IISER Mohali, Punjab, India, for providing the BET measurements used in this work.

## References

1 D. Bogdanov, A. Gulagi, M. Fasihi and C. Breyer, *Appl. Energy*, 2021, **283**, 116273.
2 V. Rosca, M. Duca, M. T. de Groot and M. T. Koper, *Chem. Rev.*, 2009, **109**, 2209–2244.
3 G. Leigh, in *Catalysts for Nitrogen Fixation*, Springer, 2004, pp. 33–54.
4 G. Soloveichik, *Nat. Catal.*, 2019, **2**, 377–380.
5 V. Kyriakou, I. Garagounis, A. Vourros, E. Vasileiou and M. Stoukides, *Joule*, 2020, **4**, 142–158.
6 M. Wang, M. A. Khan, I. Mohsin, J. Wicks, A. H. Ip, K. Z. Sumon, C.-T. Dinh, E. H. Sargent, I. D. Gates and M. G. Kibria, *Energy Environ. Sci.*, 2021, **14**, 2535–2548.
7 C. Smith, A. K. Hill and L. Torrente-Murciano, *Energy Environ. Sci.*, 2020, **13**, 331–344.
8 C. A. Fernandez and M. C. Hatzell, *J. Electrochem. Soc.*, 2020, **167**, 143504.
9 S. Ghavam, M. Vahdati, I. Wilson and P. Styring, *Front. Energy Res.*, 2021, **9**, 34.
10 U. B. Shahid, K. Siddharth and M. Shao, *Curr. Opin. Electrochem.*, 2021, **30**, 100790.
11 H. Xu, K. Ithisuphalap, Y. Li, S. Mukherjee, J. Lattimer, G. Soloveichik and G. Wu, *Nano Energy*, 2020, **69**, 104469.
12 C. Zhao, S. Zhang, M. Han, X. Zhang, Y. Liu, W. Li, C. Chen, G. Wang, H. Zhang and H. Zhao, *ACS Energy Lett.*, 2019, **4**, 377–383.
13 Q. Liu, Z. Pan, E. Wang, L. An and G. Sun, *Energy Storage Mater.*, 2020, **27**, 478–505.
14 M. Kumar and T. C. Nagaiah, *J. Mater. Chem. A*, 2022, **10**, 4720–4730.
15 X. Meng, J. Han, L. Lu, G. Qiu, Z. L. Wang and C. Sun, *Small*, 2019, **15**, 1902551.
16 X. Yang, K. Li, D. Cheng, W.-L. Pang, J. Lv, X. Chen, H.-Y. Zang, X.-L. Wu, H.-Q. Tan and Y.-H. Wang, *J. Mater. Chem. A*, 2018, **6**, 7762–7769.
17 Z. Zhao, X. Fan, J. Ding, W. Hu, C. Zhong and J. Lu, *ACS Energy Lett.*, 2019, **4**, 2259–2270.
18 G. Qing, R. Ghazfar, S. T. Jackowski, F. Habibzadeh, M. M. Ashtiani, C.-P. Chen, M. R. Smith III and T. W. Hamann, *Chem. Rev.*, 2020, **12**, 5437–5516.
19 N.-T. Suen, S.-F. Hung, Q. Quan, N. Zhang, Y.-J. Xu and H. M. Chen, *Chem. Soc. Rev.*, 2017, **46**, 337–365.
20 Z.-L. Wang, D. Xu, J.-J. Xu and X.-B. Zhang, *Chem. Soc. Rev.*, 2014, **43**, 7746–7786.
21 D. U. Lee, P. Xu, Z. P. Cano, A. G. Kashkooli, M. G. Park and Z. Chen, *J. Mater. Chem. A*, 2016, **4**, 7107–7134.
22 Y. Kong, Y. Li, B. Yang, Z. Li, Y. Yao, J. Lu, L. Lei, Z. Wen, M. Shao and Y. Hou, *J. Mater. Chem. A*, 2019, **7**, 26272–26278.
23 G. Fenya, L. Hongwei, Z. Mengzhe, X. Zhengqi, Z. Yueqing and L. Tingting, *Prog. Chem.*, 2020, **32**, 33.
24 K. Zeng, X. Zheng, C. Li, J. Yan, J. H. Tian, C. Jin, P. Strasser and R. Yang, *Adv. Funct. Mater.*, 2020, **30**, 2000503.
25 Z. Lu, J. Wang, S. Huang, Y. Hou, Y. Li, Y. Zhao, S. Mu, J. Zhang and Y. Zhao, *Nano Energy*, 2017, **42**, 334–340.
26 S. Ghosh and R. N. Basu, *Nanoscale*, 2018, **10**, 11241–11280.
27 T. Meng, J. Qin, S. Wang, D. Zhao, B. Mao and M. Cao, *J. Mater. Chem. A*, 2017, **5**, 7001–7014.
28 J. Yang, X. Wang, B. Li, L. Ma, L. Shi, Y. Xiong and H. Xu, *Adv. Funct. Mater.*, 2017, **27**, 1606497.

29 Q. Zhang, F. Luo, Y. Ling, S. Xiao, M. Li, K. Qu, Y. Wang, J. Xu, W. Cai and Z. Yang, *J. Mater. Chem. A*, 2020, **8**, 8430–8439.
30 A. Kafle, D. Gupta, A. Bordoloi and T. C. Nagaiah, *Nanoscale*, 2022, **14**, 16590–16601.
31 J. Li, F. Wei, C. Dong, Z. Wang, Z. Xiu and X. Han, *Mater. Today Energy*, 2021, 100766.
32 D. Gupta, A. Kafle, S. Kaur, P. P. Mohanty, T. Das, S. Chakraborty, R. Ahuja and T. C. Nagaiah, *J. Mater. Chem. A*, 2022, **10**, 20616–20625.
33 D. Gupta, A. Kafle and T. C. Nagaiah, *Faraday Discuss.*, 2023, DOI: 10.1039/D2FD00150K.
34 Z. Xiang, L. Li, Y. Wang and Y. Song, *Chem.–Asian J.*, 2020, **15**, 1791–1807.
35 D. Gupta, A. Kafle and T. C. Nagaiah, *Small*, 2023, 2208272.
36 S. Zhao, X. Lu, L. Wang, J. Gale and R. Amal, *Adv. Mater.*, 2019, **31**, 1805367.
37 L.-H. Zhang, F. Yu and N. R. Shiju, *ACS Sustain. Chem. Eng.*, 2021, **9**, 7687–7703.
38 D. Gupta, A. Kafle, S. Kaur, T. S Thomas, D. Mandal and T. C. Nagaiah, *ACS Appl. Mater. Interfaces*, 2023, **15**, 4033–4043.
39 D. Liu, M. Chen, X. Du, H. Ai, K. H. Lo, S. Wang, S. Chen, G. Xing, X. Wang and H. Pan, *Adv. Funct. Mater.*, 2021, **31**, 2008983.
40 S. L. Foster, S. I. P. Bakovic, R. D. Duda, S. Maheshwari, R. D. Milton, S. D. Minteer, M. J. Janik, J. N. Renner and L. F. Greenlee, *Nat. Catal.*, 2018, **1**, 490–500.
41 X. Guo, H. Du, F. Qu and J. Li, *J. Mater. Chem. A*, 2019, **7**, 3531–3543.
42 Y. Sun, X. Liu, Y. Jiang, J. Li, J. Ding, W. Hu and C. Zhong, *J. Mater. Chem. A*, 2019, **7**, 18183–18208.
43 Y. Gao, T. Zhang, Y. Mao, J. Wang and C. Sun, *J. Electroanal. Chem.*, 2023, **935**, 117315.
44 J. Bian, X. Cheng, X. Meng, J. Wang, J. Zhou, S. Li, Y. Zhang and C. Sun, *ACS Appl. Energy Mater.*, 2019, **2**, 2296–2304.
45 E. Marini, L. Jörissen and S. Brimaud, *J. Power Sources*, 2021, **482**, 228900.
46 T. C. Nagaiah, D. Gupta, S. D. Adhikary, A. Kafle and D. Mandal, *J. Mater. Chem. A*, 2021, **9**, 9228–9237.
47 S. Haller, V. Gridin, K. Hofmann, R. W. Stark, B. Albert and U. I. Kramm, *Energy Technol.*, 2021, **9**, 2001106.
48 J. Han, H. Bao, J.-Q. Wang, L. Zheng, S. Sun, Z. L. Wang and C. Sun, *Appl. Catal., B*, 2021, **280**, 119411.
49 J. Han, X. Meng, L. Lu, Z. L. Wang and C. Sun, *Nano Energy*, 2020, **72**, 104669.
50 N. Thakur, M. Kumar, D. Mandal and T. C. Nagaiah, *ACS Appl. Mater. Interfaces*, 2021, **13**, 52487–52497.
51 Z. Pu, T. Liu, G. Zhang, X. Liu, M. A. Gauthier, Z. Chen and S. Sun, *Small Methods*, 2021, **5**, 2100699.
52 L. Yi, Z. Zeng, Y. Liao, Y. Tang, X. Li, N. Lv, Y. Xu, H. Li and Y. Wang, *Energy Fuels*, 2021, **12**, 10315–10321.
53 R. K. Tripathy, A. K. Samantara and J. Behera, *Sustain. Energy Fuels*, 2021, **5**, 1184–1193.
54 S. Carenco, D. Portehault, C. Boissiere, N. Mezailles and C. Sanchez, *Chem. Rev.*, 2013, **113**, 7981–8065.
55 X. Ma, K. Zhao, Y. Sun, Y. Wang, F. Yan, X. Zhang and Y. Chen, *Catal. Sci. Technol.*, 2020, **10**, 2165–2172.
56 N. Xu, G. Cao, Z. Chen, Q. Kang, H. Dai and P. Wang, *J. Mater. Chem. A*, 2017, **5**, 12379–12384.
57 S. Gupta, M. K. Patel, A. Miotello and N. Patel, *Adv. Funct. Mater.*, 2020, **30**, 1906481.
58 V. Jose, J. M. V. Nsanzimana, H. Hu, J. Choi, X. Wang and J. M. Lee, *Adv. Energy Mater.*, 2021, **11**, 2100157.
59 Y. Xiao, C. Shen and T. Long, *Chem. Mater.*, 2021, **33**, 4023–4034.
60 X. Guo, S. Lin, J. Gu, S. Zhang, Z. Chen and S. Huang, *Adv. Funct. Mater.*, 2021, **31**, 2008056.
61 G. Qin, Q. Cui, A. Du, W. Wang and Q. Sun, *ChemCatChem*, 2019, **11**, 2624–2633.
62 S. Qi, Y. Fan, L. Zhao, W. Li and M. Zhao, *Appl. Surf. Sci.*, 2021, **536**, 147742.
63 H. Zhang, S. Wang, H. Wang, B. Huang, S. Dong, Y. Dai and W. Wei, *Nanoscale*, 2021, **13**, 17331–17339.
64 K. Elumeeva, J. Masa, D. Medina, E. Ventosa, S. Seisel, Y. U. Kayran, A. Genç, T. Bobrowski, P. Weide and J. Arbiol, *J. Mater. Chem. A*, 2017, **5**, 21122–21129.
65 X. Liu, Y. Wang, L. Chen, P. Chen, S. Jia, Y. Zhang, S. Zhou and J. Zang, *ACS Appl. Mater. Interfaces*, 2018, **10**, 37067–37078.
66 J.-l. Ma, N. Li, Q. Zhang, X.-b. Zhang, J. Wang, K. Li, X.-f. Hao and J.-m. Yan, *Energy Environ. Sci.*, 2018, **11**, 2833–2838.
67 H. Park, A. Encinas, J. P. Scheifers, Y. Zhang and B. P. Fokwa, *Angew. Chem., Int. Ed.*, 2017, **56**, 5575–5578.
68 H. Xu, B. W. Zeiger and K. S. Suslick, *Chem. Soc. Rev.*, 2013, **42**, 2555–2567.
69 B. Coşkuner, A. K. Figen and S. Pişkin, *J. Chem.*, 2014, **2014**, 185957.
70 Z. Li, T. Zhuang, J. Dong, L. Wang, J. Xia, H. Wang, X. Cui and Z. Wang, *Ultrason. Sonochem.*, 2021, **71**, 105384.
71 U. B. Shahid, Y. Chen, S. Gu, W. Li and M. Shao, *Trends Chem.*, 2021, **4**, 142–156.
72 J.-T. Ren, L. Chen, Y. Liu and Z.-Y. Yuan, *J. Mater. Chem. A*, 2021, **9**, 11370–11380.
73 W. Lei, D. Portehault, D. Liu, S. Qin and Y. Chen, *Nat. Commun.*, 2013, **4**, 1–7.
74 Y. Zhao, R. Shi, X. Bian, C. Zhou, Y. Zhao, S. Zhang, F. Wu, G. I. Waterhouse, L. Z. Wu and C. H. Tung, *Adv. Sci.*, 2019, **6**, 1802109.
75 J. Choi, B. H. Suryanto, D. Wang, H.-L. Du, R. Y. Hodgetts, F. M. F. Vallana, D. R. MacFarlane and A. N. Simonov, *Nat. Commun.*, 2020, **11**, 1–10.
76 D. Ekeberg, G. Ogner, M. Fongen, E. J. Joner and T. Wickstrøm, *J. Environ. Monit.*, 2004, **6**, 621–623.
77 J. Masa, P. Weide, D. Peeters, I. Sinev, W. Xia, Z. Sun, C. Somsen, M. Muhler and W. Schuhmann, *Adv. Energy Mater.*, 2016, **6**, 1502313.
78 Y. Tsarfati, S. Rosenne, H. Weissman, L. J. Shimon, D. Gur, B. A. Palmer and B. Rybtchinski, *ACS Cent. Sci.*, 2018, **4**, 1031–1036.
79 B. Jiang, H. Song, Y. Kang, S. Wang, Q. Wang, X. Zhou, K. Kani, Y. Guo, J. Ye and H. Li, *Chem. Sci.*, 2020, **11**, 791–796.

 

80 G. Arzac, T. C. Rojas and A. Fernández, *ChemCatChem*, 2011, **3**, 1305–1313.
81 B. Guan, L. Fan, X. Wu, P. Wang, Y. Qiu, M. Wang, Z. Guo, N. Zhang and K. Sun, *J. Mater. Chem. A*, 2018, **6**, 24045–24049.
82 V. A. Sethuraman, J. W. Weidner, A. T. Haug, M. Pemberton and L. V. Protsailo, *Electrochim. Acta*, 2009, **54**, 5571–5582.
83 J. M. V. Nsanzimana, Y. Peng, Y. Y. Xu, L. Thia, C. Wang, B. Y. Xia and X. Wang, *Adv. Energy Mater.*, 2018, **8**, 1701475.
84 L. Cui, W. Zhang, R. Zheng and J. Liu, *Chem.–Eur. J.*, 2020, **26**, 11661–11672.